

## Effect of annealing treatment on mechanical and fatigue properties of Inconel 718 alloy melted by selective laser melting

Lei Li<sup>1</sup>, Xujun Zhu<sup>1</sup> , Fuzheng Tian<sup>1</sup>, Yun Chen<sup>1</sup>, Qiao Liu<sup>1</sup>

<sup>1</sup>Inner Mongolia University of Technology, College of Sciences. 49 Aimin Street, Xincheng District, 010051, Hohhot, PR China.

e-mail: leillt@163.com, zhuxujun81@163.com, 229677172@qq.com, 2089444176@qq.com, 1097555026@qq.com

### ABSTRACT

Inconel 718 alloy which was prepared using selective laser melting (SLM) forming technology underwent various annealing treatments. Optical microscope, scanning electron microscope, electron backscattered diffraction and MTS testing machine were used to study the microstructure, mechanical and fatigue properties of Inconel 718 alloy melted by selective laser melting under different annealing treatments. The results show that the microstructure of Inconel 718 alloy after homogenization and double aging annealing is the most obvious, and the microstructure of the alloy is mainly recrystallized. The microstructure contains a large number of annealing twins and the grain boundaries are flat. The yield strength, tensile strength and microhardness of Inconel 718 alloy formed by selective laser melting after different annealing treatments are greatly increased, while the elongation after fracture is significantly decreased. The fatigue properties of Inconel 718 alloy after double aging annealing and solution dual aging annealing are improved slightly, while the fatigue properties after uniform double aging annealing are decreased slightly.

**Keywords:** Selective laser melting; Inconel 718; Microstructure; Mechanical properties; Fatigue properties.

### 1. INTRODUCTION

Inconel 718 alloy is a nickel-based superalloy with good corrosion resistance, oxidation resistance, fatigue resistance and high-temperature mechanical properties. It is an indispensable structural material for energy, power, aerospace, and other industrial fields [1–3]. However, the Inconel 718 alloy manufactured by traditional methods has limitations and cannot meet the requirements of complex shapes and high dimensional accuracy of Inconel 718 alloy parts [4, 5]. The Inconel 718 alloy parts were fabricated using additive manufacturing (AM) technology, which effectively solved the processing challenges [6].

Selective laser melting (SLM) is an additive manufacturing technology that selectively fuses powder layers in a protective atmosphere using computer-controlled laser beams to obtain a nearly net-like structure [7]. Due to the flexibility of geometric design and faster forming speed, it has been widely used in the processing and manufacturing of Inconel 718 alloys, breaking the limitation of part structure by conventional processes [8, 9]. However, in the SLM forming process, accompanied by repeated thermal cycling processes, such as repeated melting and rapid solidification [10], the produced Inconel 718 alloy has significant microstructure inhomogeneity and segregation problems, and annealing treatment is usually adopted to improve its microstructure and mechanical properties [11].

ZHANG *et al.* [12] performed solid solution, homogenization and dual aging annealing treatments on SLM Inconel 718 alloy with reference to the heat treatment regime for cast and wrought Inconel 718 alloys. The results show that the strength and hardness of Inconel 718 alloy are increased after different annealing treatments, while the elongation after different annealing treatments is decreased, and the toughness are larger and deeper. ZHANG *et al.* [13] conducted various aging heat treatments on Inconel 718 alloy fabricated with SLM and found that the microhardness and tensile strength increased initially and then decreased with time after different aging temperature treatments. The higher the aging temperature, the shorter the aging time required to reach the maximum hardness and strength. SHI *et al.* [14] studied the effect of solid solution time on Inconel 718 alloy formed by SLM, and found that the grain size of the alloy increased after solid solution treatment, and the fraction of small-diameter grains decreased with the increase of solid solution time. The durability of the alloy after solid solution treatment is improved, and on the elongation is decreased slightly. YOO *et al.* [15]

performed stress relief annealing on SLM Inconel 718 alloy by stress relief annealing and solution aging heat treatment, and the two treatments produced different microstructures. After stress relief annealing the dendritic grain boundaries disappears, and the stress concentrated at the grain boundaries. However, a large number of precipitates and annealing twins appear in the solution-aging treatment The grains of alloy after stress-relief annealing are finer and the strength is higher. GALLMEYER *et al.* [16] treated SLM Inconel 718 alloy through the standard heat treatment, direct aging, and optimized multi-step heat treatment. Their results show that the heat-treated Inconel 718 alloy outperforms the wrought and printed alloys.

At present, the annealing system of SLM Inconel 718 alloy is still in the exploratory stage. In present paper, we have selected three kinds of annealing heat treatments for this alloy including (a) direct double-aging annealing, (b) two-stage annealing treatment, solution and double-aging annealing, and (c) two-stage annealing treatment, homogenization and double aging annealing. Optical microscopy (OM), scanning electron microscopy (SEM), and electron backscatter diffraction (EBSD) were applied to study the microstructure, mechanical and fatigue properties of Inconel 718 alloy formed by SLM under different annealing treatments. This work will a foundation for further study on perfecting and optimizing the annealing treatment system of Inconel 718 alloy formed by SLM and shed some light on the mechanisms of its fatigue fracture.

## 2. EXPERIMENTAL MATERIALS AND METHODS

In this experiment, the EP-M250 equipment was used to prepare Inconel 718 alloy by laser selective melting and forming, and its chemical composition is shown in Table 1. The machine was used to directly print bone shaped specimens for mechanical property testing, defining the Z-axis parallel to the building direction and taking the X-Y plane as the base plane. Strip scanning was carried out under the protection of argon gas. In order to release the residual stress between the substrate and the sample during printing, the substrate was preheated to 80°C in advance. The laser power and scanning speed are 285W and 960mm/s respectively. For each subsequent layer, the laser scan path was rotated 67° counterclockwise. The diagram and parameters of the SLM process are shown in Figure 1.

**Table 1:** Chemical composition (%) of Inconel 718.

C	Si	Mn	S	P	Cr	Ni
0.05	0.043	0.03	0.002	0.034	19.01	52.30
Al	Nb	Ti	Cu	B	Mo	Fe
0.57	5.07	1.00	0.02	0.003	3.06	Bal

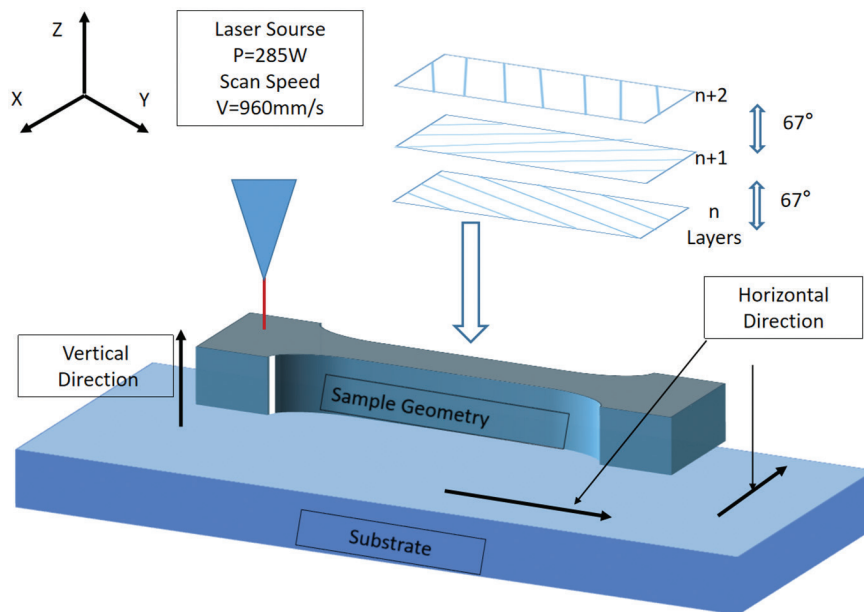


**Figure 1:** Schematic diagram of the SLM process.

**Table 2:** Annealing Treatment Process of the samples.

SAMPLE	ANNEALING TREATMENT PROCESS
AT1	720°C × 8h / FC + 620 × 8h / AC (Double-Aging)
AT2	980°C × 1.5h / AC + 720°C × 8h / FC + 620 × 8h / AC (Solution + Double-Aging)
AT3	1080°C × 1.5h / AC + 720°C × 8h / FC + 620 × 8h / AC (Homogenization + Double-Aging)

Note: FC: furnace cooling, AC: air cooling.

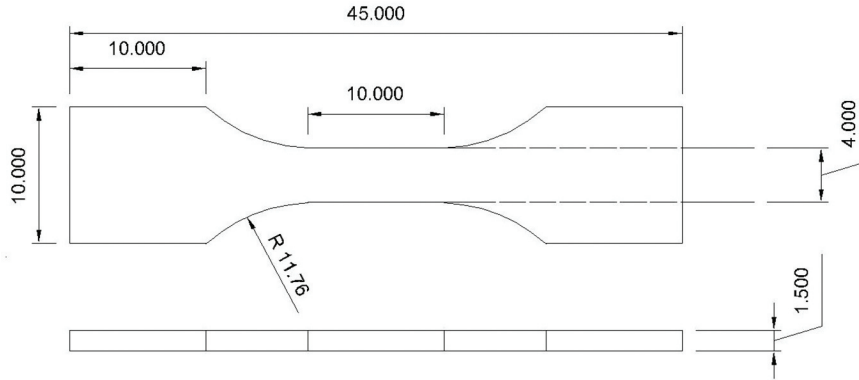


**Figure 2:** Schematic of sample diagram(mm).

To avoid the influence of the upper molten surface on the material properties after SLM forming, the upper molten surface of the SLM Inconel 718 alloy was removed and machined to a uniform size using a wire cutter (DK7740). The final shape and dimension of the specimens for mechanical testings are shown in Figure 2. The machined Inconel 718 alloy was annealed and the annealing experimental protocol for the SLM Inconel 718 alloy is listed in Table 2.

Uniaxial tensile tests were performed on SLM Inconel 718 alloy with different annealing treatments at room temperature with a hydraulic servo MTS testing machine at a tensile rate of 1mm/min. Uniaxial tensile fatigue tests were carried out under different stress levels, the fatigue loading stress ratio was  $R = 0.1$ , and the fatigue frequency was 10Hz.

The specimens were subjected to Vickers hardness measurement using a digital microhardness tester (AHVD-1000XY) with a load of 1000gf and a load retention time of 10 seconds. 10 measurement points were taken for each sample, and the maximum and minimum values were removed to calculate the average value.

The X-Y surface of the SLM Inconel 718 alloy was sanded using 400~3000 grit sandpaper, followed by mechanical polishing and metallographic etching. The ratio of metallographic etching solution is  $HCl:C_2H_5OH:-CuCl_2 = 20ml:20ml:1g$ . The microstructure of the corroded samples was observed under optical microscope and scanning electron microscope. Electrolytic polishing of SLM Inconel 718 alloy was carried out with a 10% perchlorate alcohol solution. During electrolytic polishing, the temperature was kept at  $-20\sim-30^\circ C$ , the voltage was 25V, the current was 0.26A, and the time was 60s. EBSD analysis was conducted on the electrolytic polished samples. Channel 5 software was used to post-process EBSD data and extract the microstructure information. The fracture morphologies of tension and fatigue specimens were observed by scanning electron microscope.

### 3. RESULTS AND DISCUSSIONS

#### 3.1. Microstructure

The microstructure of the as-deposited SLM Inconel 718 Alloy is distinctly different from that of the as-cast and wrought alloys [17]. Figure 3 shows the X-Y microstructure of the as-deposited SLM Inconel 718 alloy. As shown in the Figures 3a and 3b, the selected interlayer angle is  $67^\circ$ , which is more compact than other interlayer angles. In the figure, the metallurgical bond between adjacent molten channels of the samples is almost no significant defects such as pores. When the SLM is formed, the adjacent channels are scanned a second time due to the strip scanning. The solidified metal in the area is re-melted and re-cooled at different rates by the second scan, resulting in the dendrite morphology changes alternately along the laser scan path. Supersaturated Nb-rich solid solution tends to form in the liquid to be cured in the remelted region during the secondary scan, so the

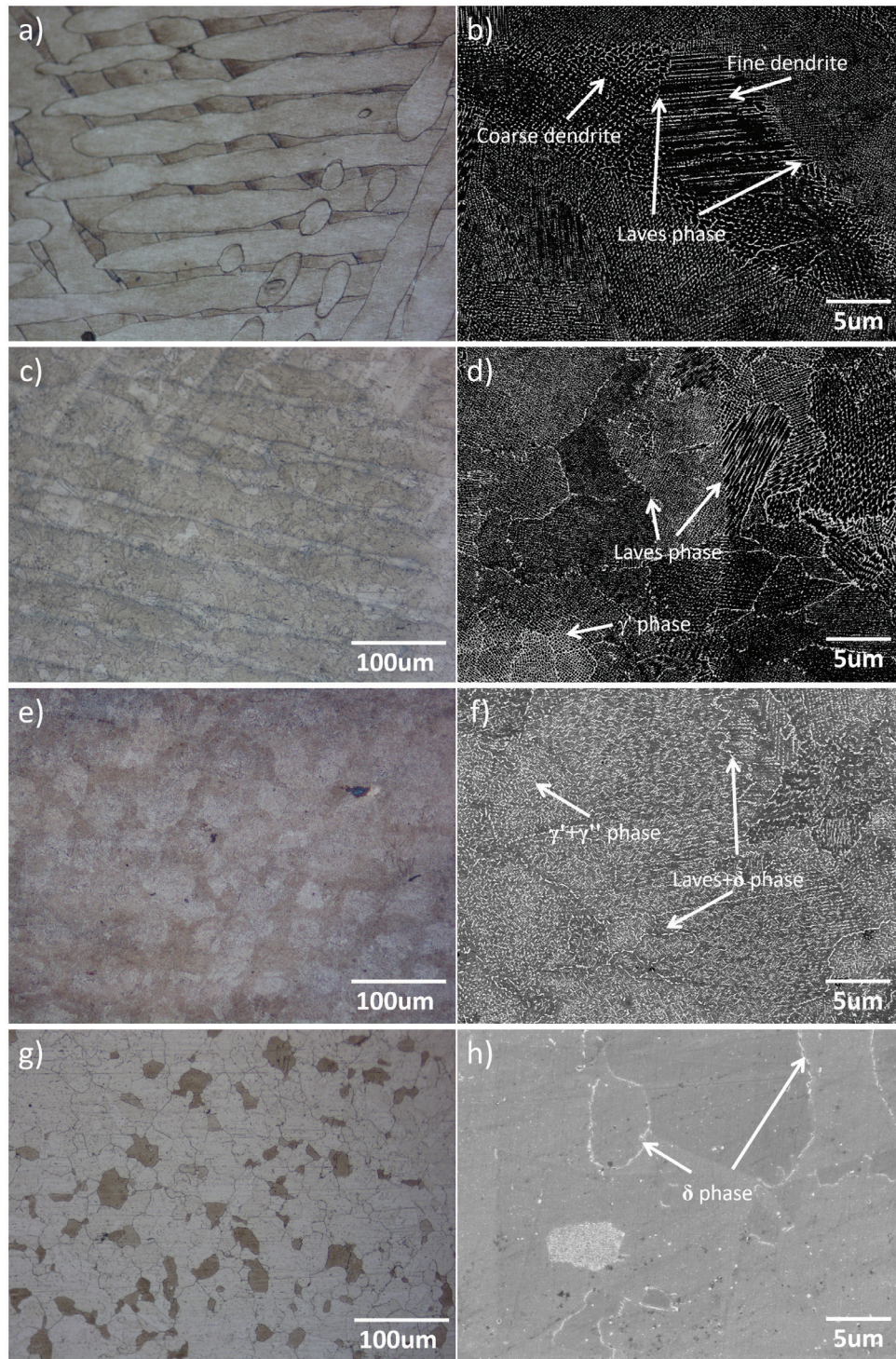


**Figure 3:** Microstructure of SLM fabricated Inconel 718 alloy with various annealing treatment. (a, b) As-deposited, (c, d) AT1, (e, f) AT2, (g, h) AT3.

Laves phase also tends to precipitate at the overlap between adjacent melt paths [18]. Figures 3c and 3d show the microstructure of the AT1 specimen. After the double aging annealing treatment, the SLM Inconel 718 alloy starts to fuse between the adjacent melt channels and the melt marks become blurred. At the same time, the ring or strip of Laves phase is distributed among the dendrites, and a large amount of  $\gamma'$  phase is precipitated in the grain. Figures 3e and 3f show the microstructure of the AT2 specimen. After solid solution plus double aging annealing treatment, the melt scar structure of SLM Inconel 718 alloy disappears completely, and the internal organization consists of columnar crystal and dendrite structure with relatively coarse grain structure. A large amount of  $\gamma'$  and  $\gamma''$  phases precipitate inside the crystal, and the dissolved  $\delta$  phase of Laves phase precipitate at

the grain boundary. The microstructure of specimen with AT3 was shown in Figures 3g and 3h. After homogenization and double aging annealing, the internal columnar crystal and dendrite structure of SLM Inconel 718 alloy completely disappear and is transformed into uniform equiaxed massive crystals with coarsened grain boundaries that are obvious and straight, and only some  $\delta$  phase precipitates at the grain boundaries.

Figure 4 shows the EBSD orientation imaging morphology (Inverse pole figure, IPF) of SLM Inconel 718 alloy after different annealing treatments. It can be seen from Figure 4a that after the direct double-aging annealing treatment, the grains grow in the  $\langle 001 \rangle$  direction (the red part in the figure) in the unremelted region, while in the remelted region, the heat flow diffuses into the surrounding solidified metal with complex and changeable direction, leading to both parallel growing columnar crystals and equiaxed crystals of different sizes. The orientation difference between different grains is large, which destroys the columnar crystals in the dominant orientation of  $\langle 001 \rangle$  direction [19]. As can be seen from Figure 4b, the solid solution treated with double-aging annealing exhibits a “checkerboard” microstructure with a more uniform grain size distribution than that in the AT1 specimen, but no significant change in the grain orientation pattern. From Figure 4c, it can be seen that the internal structure of the alloy has undergone significant changes, where the internal grains have become coarser, and the grain boundaries have become flatter. Many annealed twins can be seen in the figure, and orientation twin boundaries appear in a large number of high-angle material, indicating that the orientation difference between grains in the internal grains of the material increases.

Figure 5 shows the grain size of SLM Inconel 718 alloy after different annealing treatments. The length and width of the grains were counted using the truncated line method. Result shows that the grain size of SLM Inconel 718 alloy increases with the annealing treatment from AT1 to AT3. Figure 6 shows the orientation difference angles of SLM Inconel 718 alloy after different annealing treatments. The interior of AT1 specimen is mainly composed of small-angle grain boundaries. The interior of AT2 specimen is also composed of small-angle grain boundaries, but its grain boundary difference angle is slightly larger than that of AT1 specimen. The interior of AT3 specimen is mainly composed of large-angle grain boundaries. The disappearance of small-angle grain

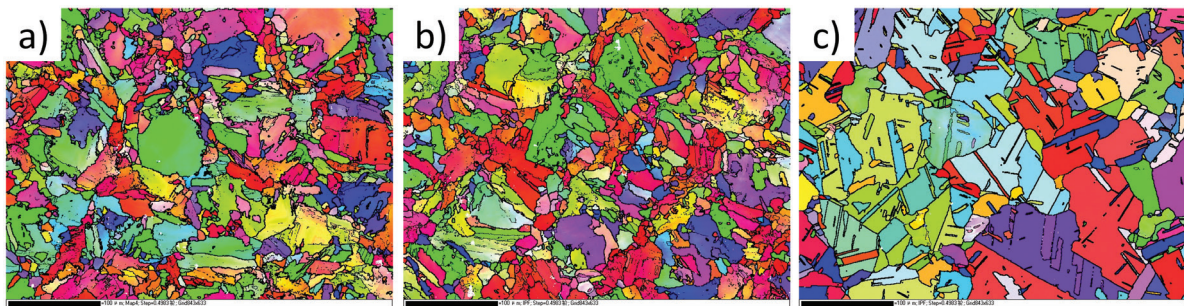


Figure 4: IPF images of different annealing treatment samples showing grain structures. (a) AT1, (b) AT2, (c) AT3.

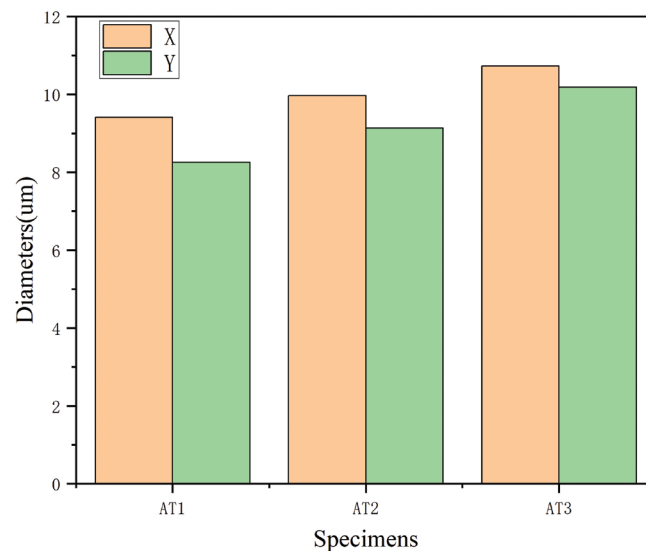


Figure 5: Grain size diagram of different annealing treatment samples showing coarsening.

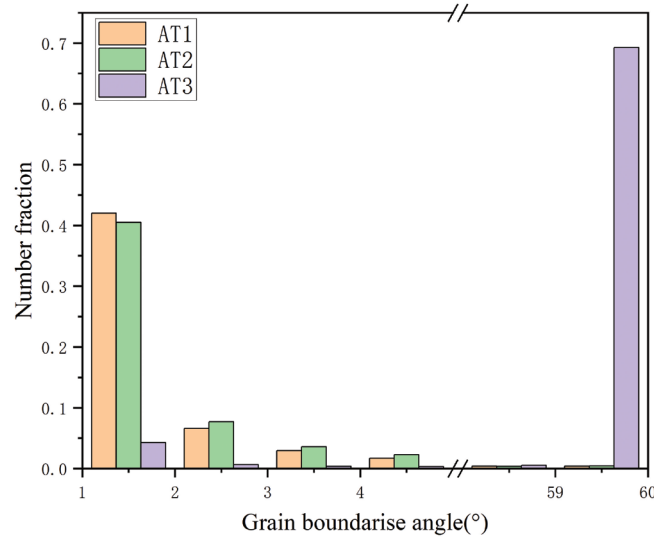


Figure 6: Grain boundaries angle diagram of different annealing treatment samples.

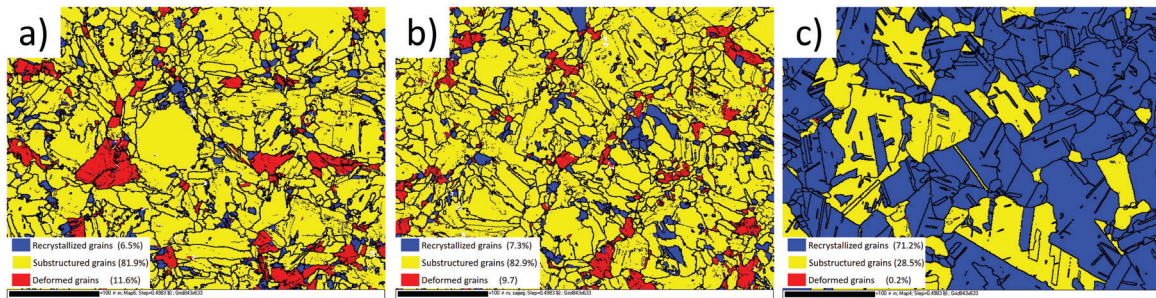


Figure 7: Distribution of recrystallization microstructure in different annealing treatment samples. (a) AT1, (b) AT2, (c) AT3.

boundaries inside the grains indicates that the non-equilibrium organization inside the SLM Inconel 718 alloy has recrystallized and a large number of 60° annealed twins have appeared.

Figure 7 shows the distribution recrystallized microstructure of SLM Inconel 718 alloy after different annealing treatments. It can be seen from Figures 7a and 7b that the internal microstructure distribution after the direct double-aging annealing treatment and the solid solution double-aging annealing treatment is almost the same, both with mainly substructure containing a small amount of deformed and recrystallized grains. Figure 7c shows that the internal structure of the alloy is dominated by recrystallized grains and contains a large number of substructures, and the deformed grains almost disappear after homogenous double-aging annealing. At 1080°C, the undistorted nuclei inside the columnar crystals grow to form sub-grain or recrystallized grains, and similar sub-grain boundaries are transferred to adjacent grain boundaries or sub-grain boundaries through slippage. Furthermore, two or more sub-grains combine into a recrystallized grain through diffusion and other means, and thus the grains grow. At this time, the structure is uniform and the grain boundaries are flat [20]. Recrystallization, substructure and deformed grains are observed in AT1 specimen. The volume fractions of recrystallized, substructured and deformed grains in AT1 specimen are 6.5%, 81.9%, and 11.6%, respectively. Similarly, the volume fractions of recrystallized, substructured and deformed grains in AT2 specimen are 7.3%, 82.9%, and 9.7%, respectively. In contrast, the volume fractions of recrystallized, substructured and deformed grains in AT3 specimen are 71.2%, 28.5%, and 0.2%, respectively.

### 3.2. Mechanical properties

The engineering stress-strain curves of SLM Inconel 718 alloy in the deposited state and after annealing treatment are shown in Figure 8, and the mechanical properties of SLM Inconel 718 alloy in the deposited state and after annealing treatment are summarized in Table 3. It can be seen that after the annealing treatment, the yield strength and tensile strength of the alloy are increased to different extent, and the elongation is decreased. After

**Table 3:** Mechanical properties of SLM Inconel 718 alloys under various annealing treatments.

SAMPLE	YIELD STRENGTH (MPa)	TENSILE STRENGTH (MPa)	FRACTURE ELONGATION (%)	VICKERS HARDNESS (HV)
As-deposited	762 ± 10	1003 ± 8	21.7 ± 2	311
AT1	1130 ± 14	1400 ± 12	13.6 ± 1	493
AT2	1200 ± 22	1504 ± 20	9.8 ± 0.7	453
AT3	970 ± 7	1379 ± 5	18.4 ± 1.6	460

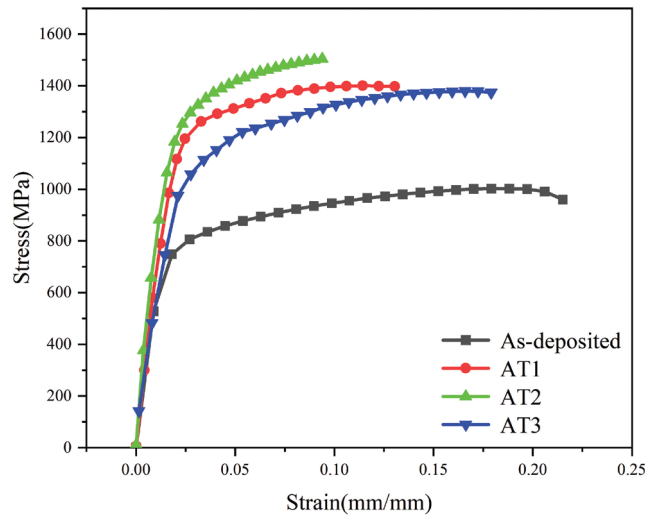


**Figure 8:** Stress-strain curves of SLM Inconel 718 alloys under various annealing treatments.

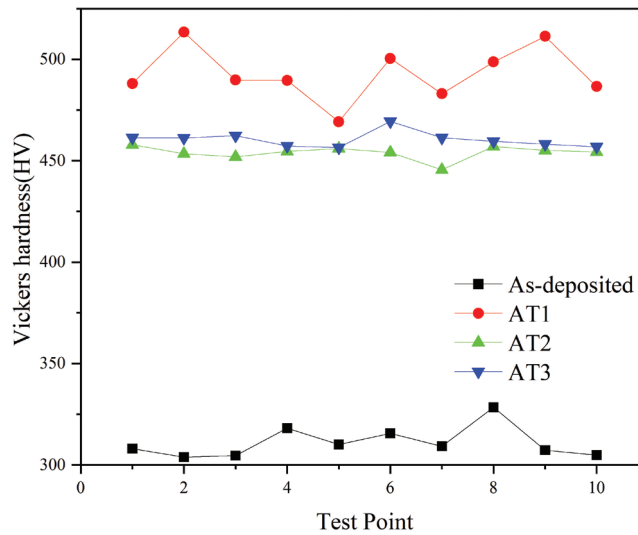


**Figure 9:** Surface micro-hardness curves of SLM Inconel 718 alloys under various annealing treatments.

direct double-aging annealing, the yield strength and tensile strength of the alloy increase by 48.3% and 39.6% compared with the deposited state, and the elongation decreases by 37.3%. The most significant increase in strength is achieved after solid solution plus double aging annealing, with yield and tensile strengths increasing by 57.5% and 49.9%, respectively, compared to the deposited state, but the most significant decrease of 54.8% in elongation is also observed at the same time, with a decrease. Under double aging annealing treatment, the yield strength and tensile strength of the alloy after homogenization increase by 27.3% and 37.5% compared with the deposited state, and the elongation decrease by only 15.2%. Figure 9 shows the surface hardness curves of SLM Inconel 718 alloy. Compared with the as-deposited state, the hardness of the annealed SLM Inconel

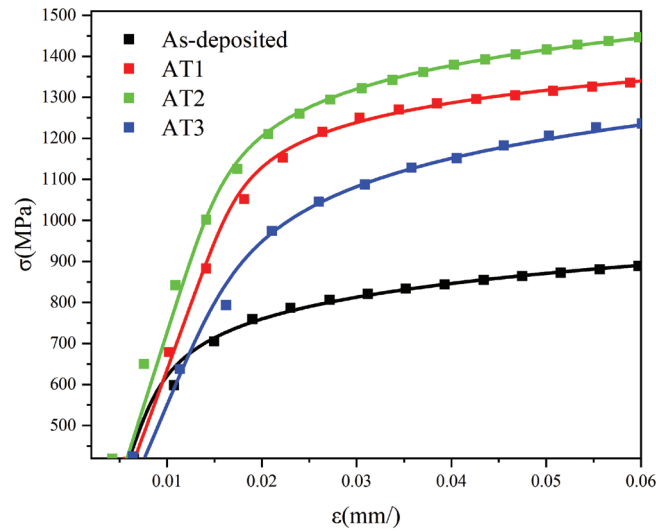


**Figure 10:** Curve-fitting of axial tensile stress-strain relationship of SLM Inconel 718 alloys.

718 alloy increases significantly. a maximum of 493HV achieved under AT1, which is 58.5% higher than that of the deposited state. The hardnesses of AT2 and AT3 specimens are 453HV and 461HV respectively, which are 45.6% and 47.9% higher than the deposited state.

All the annealing treatments involved increase the strength and degrade ductility, among which the AT3 gives the best performance by greatly raise the strength with a slight decrease of elongation. The mechanical properties of SLM Inconel 718 alloy changed to different degrees after different annealing treatments. These variations can be attributed to three main strengthening mechanisms of SLM Inconel 718 alloy: (a) Age strengthening. Following theage annealing treatment in SLM Inconel 718 alloy, then, the second phase in the alloy precipitates and grows, and these second phases hinder the movement of crystal dislocations during the hardening process of the material, thus increasing its yield and tensile strength of the material [21]; (b) Solution strengthening. Following the solid solution annealing treatment of SLM Inconel 718 alloy, the Laves phase in the alloy decomposes to release solute elements [22], and these solute elements are then incorporated into the solid solution, resulting in lattice distortion. The inhomogeneous lattice hinders the movement of crystal dislocations and causes the plastic deformation of the alloy more difficult, thus increases the yield strength and tensile strength of the alloy; (c) Grain boundary strengthening. The grain boundaries increases the strength of the material by hindering the movement of dislocations. After annealing, recrystallization occurs, and a large number of recrystallized grains increase the number of grain boundaries, meanwhile, a large number of high-angle twin grain boundaries are generated, which the crystal slip is obstructed, resulting in the improvement of alloy strength [23].

The uniaxial tensile stress-strain relationship of SLM Inconel 718 alloy can be represented by the Ramberg-Osgood model, and the fitted results of the Ramberg-Osgood model are shown in Figure 10.

$$\varepsilon = \frac{\sigma}{E} + \left( \frac{\sigma}{K} \right)^{1/n} \tag{1}$$

where  $K$  is the plastic strength of the alloy and  $n$  is the plastic hardening index of the alloy. The best-fit  $K$  and  $n$  of the as-deposited state are 1197 MPa and 0.1016, respectively; the best-fit  $K$  and  $n$  of the AT1 specimen are 1649MPa and 0.0753, respectively; the best-fit  $K$  and  $n$  of the AT2 specimen are 1740MPa and 0.0653, respectively; and the best-fit  $K$  and  $n$  of the AT3 specimen are 1600MPa and 0.0972, respectively. These parameters indicate that the uniaxial stress-strain behavior of SLM Inconel 718 alloys have similar uniaxial tensile stress-strain behavior after different annealing treatments. The smaller the plastic hardening index of an alloy, the higher the strength. The ability to rely on hardening to deform the material uniformly is weaker, and the less the hardness increases after fracture. The plastic hardening index  $n$  (deposited state > AT3 > AT1 > AT2) is measured experimentally, and the hardness of the alloy after fracture increases by 103 HV for the deposited state specimen, 31 HV for the AT1 specimen, 21 HV for the AT2 specimen, and 74 HV for the AT3 specimen. verified the variation pattern of the fitted parameters.

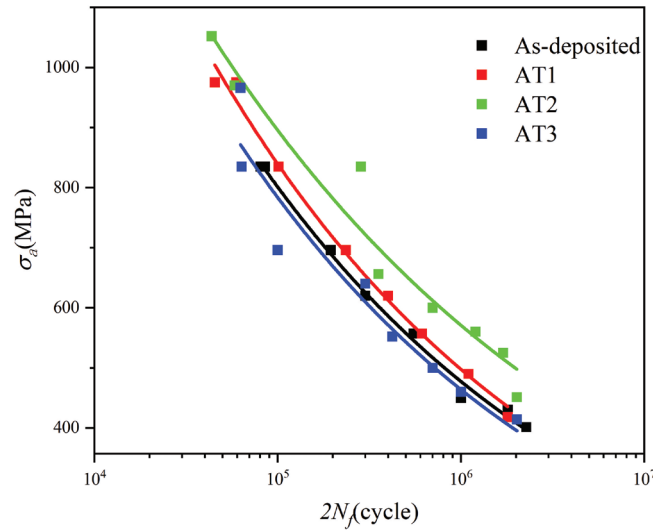


**Figure 11:** Fatigue life curves for SLM Inconel 718 alloys under various annealing treatments.

**Table 4:** The values of the Basquin parameters in SLM Inconel 718 alloys.

SAMPLE	$\sigma_f$ (MPa)	$b$
As-deposited	9722	-0.22484
AT1	10359	-0.2271
AT2	10738	-0.19544
AT3	7215	-0.2277

### 3.3. Fatigue properties

Fatigue tests were carried out under given constant stress amplitudes converted from different stress levels selected based on the tensile strength of SLM Inconel 718 alloy. Figure 11 shows results of stress-controlled fatigue tests of SLM Inconel 718 alloy with all loading ratios  $R = 0.1$ . In order to characterize the fatigue behavior of SLM Inconel 718 alloy, the Basquin equation [24] was used to fit the  $S-N$  fatigue life.

$$\sigma_a = \sigma_f (2N_f)^b \tag{2}$$

Where  $\sigma_f$  is the fatigue strength coefficient (MPa),  $N_f$  is the number of cycles to failure, and  $B$  is the Basquin index. The fitting parameters of the fatigue performance model are shown in Table 4. The results show that under the same stress amplitude, the fatigue properties of the annealed specimens are significantly higher than that of the deposited specimens, except for the AT3 specimens. However, under the same stress level, the fatigue properties of the deposited specimens are distinctly better than those of the annealed specimens.

Fatigue performance is more dependent on the microstructure of the materials than static strength. The annealed SLM Inconel 718 alloy has higher static strength, but it is very important to understand the fatigue mechanism of SLM Inconel 718 alloy after different annealing treatments and to clarify the fatigue properties of SLM Inconel 718 alloy after different annealing treatments.

Figure 12 shows the fatigue fracture morphologies of SLM Inconel 718 alloy in the as-deposited state and under different annealing treatment schemes. The fatigue fracture morphology is divided into fatigue crack initiation zone (FCIZ), fatigue crack propagation zone (FCPZ), and final rupture zone (FRZ). It is clear from Figures 12a–d that the fatigue fracture morphologies of all SLM Inconel 718 alloys are composed of fatigue crack initiation and fatigue crack propagation and the final rupture zone. It can be seen from Figure 12e that the fatigue cracks in the deposited state start from a pore defect near the surface of the specimen and extend inward; it can be seen from Figure 12f, h that the fatigue cracks in the AT1 and AT3 specimens start from a defect at the surface attachment and extend to the interior of the specimen; it can be seen from Figure 12g that the fatigue cracks in the AT2 specimens start from an inclusion particles near the surface and extend to the interior of the

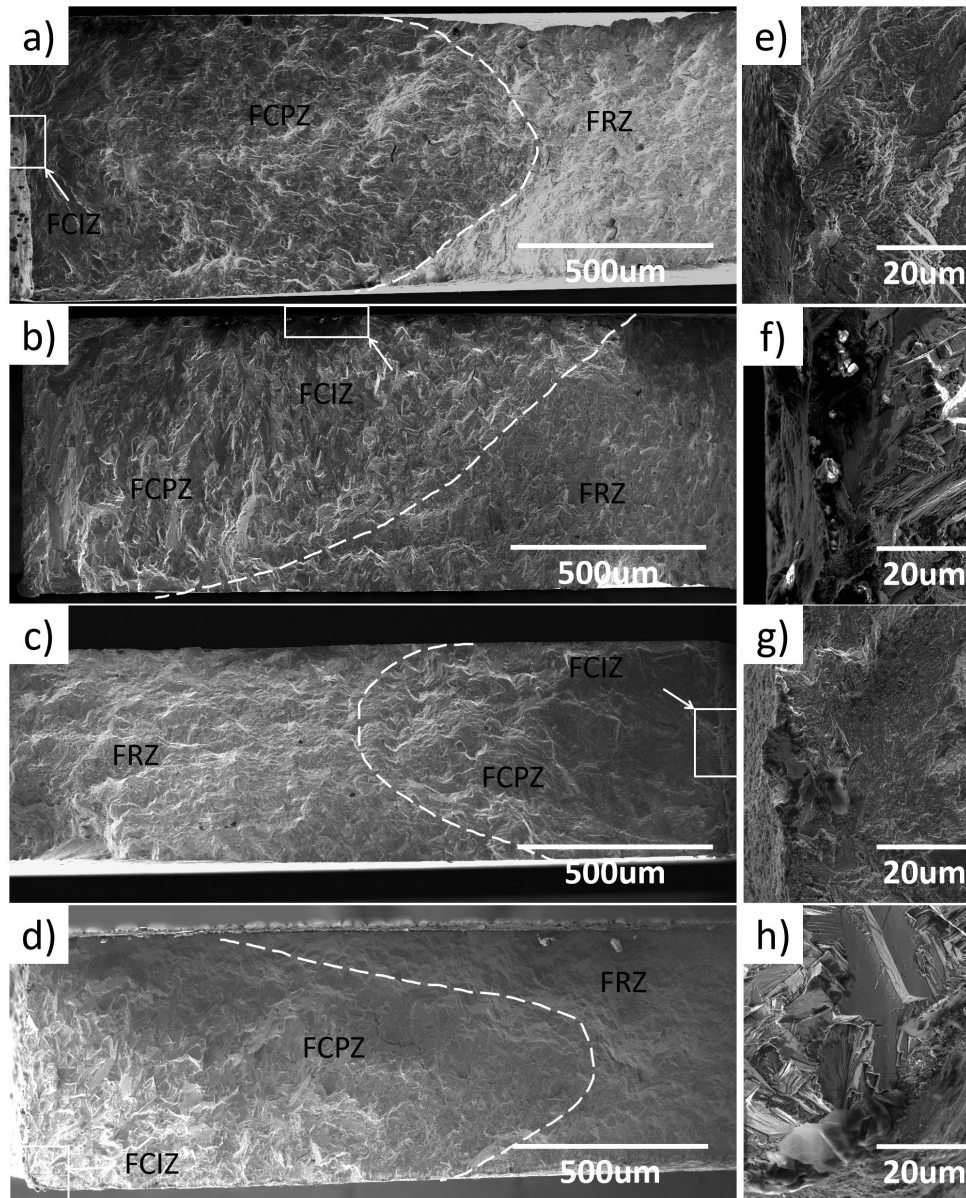


**Figure 12:** Fatigue fracture morphology of SLM Inconel 718 alloys under various annealing treatments. (a, e) As-deposited, (b, f) AT1, (c, g) AT2, (d, h) AT3.

specimen. Before and after annealing, the fatigue cracks started from the surface of the specimen, or from the defects near the surface of the specimen and propagated into the interior of the specimen. It indicates that although processes such as machining, polishing, and annealing reduce the effect of surface roughness and associated notch effects, residual pores and defects inside the alloy still play a dominant role in the fatigue damage process [25].

In addition to the conventional fracture properties shown in Figure 12 and Figure 13 also shows the typical morphology of the SLM Inconel 718 alloy in the final fracture zone. As shown in Figure 13, the fracture morphology of the transient fracture zone of the deposited specimen exhibits the characteristics of static tensile fracture, which is composed of a large number of tough nests and tearing ridges. These features are the same as that of in the AT1 specimen, but the tough nests in the deposited specimen are smaller and deeper. It indicates that the elongation after fracture of the deposited specimen is better than that of the AT1 specimen [26], which is consistent with the above tensile test results. In addition to a large number of dimples, some small tear ridges and a small number of cleavage planes were observed in AT2 sample, which still showed ductile fracture macroscopically. In addition to dimples, large areas of cleavage planes were observed in AT3 sample. Furthermore, some cleavage planes were distributed on the fracture

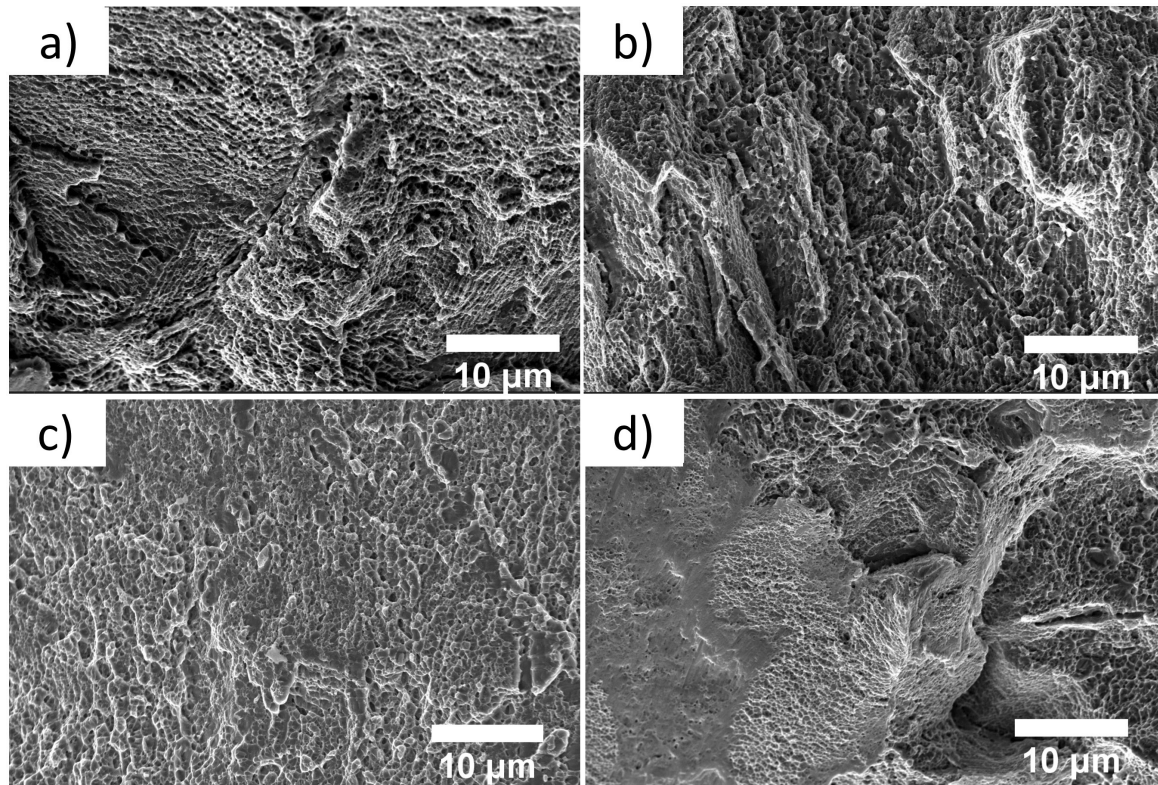


**Figure 13:** Morphology of the final fracture zone of SLM Inconel 718 alloys under various annealing treatments. (a) As-deposited, (b) AT1, (c) AT2, (d) AT3.

surface, and some tear ridges were generated at the edges of those cleavage planes. The large number of cleavage planes reduced the toughness of the material, resulting in a decrease in the fatigue properties of the AT3 sample.

#### 4. CONCLUSIONS

After double-aging annealing treatment and solid solution aging heat treatment, the microstructure of SLM Inconel 718 alloy did not change significantly, and it was composed of equiaxed crystals. When the internal recrystallization changes, the internal structure is uniform, the grain boundaries are straight, and a large number of annealed twins appear.

After various annealing treatment, the properties of SLM Inconel 718 alloy were improved to different degrees. The hardness of SLM Inconel 718 alloy is 493HV after double-aging annealing, and the yield strength and tensile strength are 1130MPa and 1400MPa respectively; SLM Inconel 718 alloy after solid solution aging has the maximum yield strength and tensile strength, 1200MPa and 1504MPa respectively, but its elongation is only 9.8%. After homogenization aging annealing, SLM Inconel 718 alloy has the highest yield strength and tensile strength with only a small decrease in elongation and a high hardness.

The fatigue cracks of SLM Inconel 718 alloy are all initiated on or close to the surface, and the fatigue performance of SLM Inconel 718 alloy after solution aging treatment is the best.

#### 5. ACKNOWLEDGMENTS

This work was supported by the Doctoral Fund of Inner Mongolia University of Technology [grant numbers BS2021053]; Research Projects of Universities in Inner Mongolia Autonomous Region [grant numbers JY20220254]; and the National Natural Science Foundation of China [grant numbers 12262029].

#### 6. BIBLIOGRAPHY

- [1] WARREN, J., WEI, D.Y., "The cyclic fatigue behavior of direct age 718 at 149, 315, 454 and 538 °C", *Materials Science and Engineering*, v. 428, n. 1-2, pp. 106–115, 2006. doi: <http://dx.doi.org/10.1016/j.msea.2006.04.091>.

- [2] SHI, C., ZHONG, Z., “Development and innovation of superalloy in China”, *Chin Shu Hsueh Pao*, v. 46, n. 11, pp. 1281–1288, 2010. doi: <http://dx.doi.org/10.3724/SP.J.1037.2010.01281>.
- [3] ZHANG, Y., YANG, L., CHEN, T., *et al.*, “Investigation on the optimized heat treatment procedure for laser fabricated IN718 alloy”, *Optics & Laser Technology*, v. 97, pp. 172–179, Dec. 2017. doi: <http://dx.doi.org/10.1016/j.optlastec.2017.06.027>.
- [4] SEOW, C.E., COULES, H.E., WU, G., *et al.*, “Wire+Arc Additively Manufactured Inconel 718: effect of post-deposition heat treatments on microstructure and tensile properties”, *Materials & Design*, v. 183, pp. 108157, Dec. 2019. doi: <http://dx.doi.org/10.1016/j.matdes.2019.108157>.
- [5] WANG, X., WANG, X., ZHAI, J., *et al.*, “Improvement to flooding risk assessment of storm surges by residual interpolation in the coastal areas of Guangdong Province, China”, *Quaternary International*, v. 453, pp. 1–14, Sep. 2017. doi: <http://dx.doi.org/10.1016/j.quaint.2016.12.025>.
- [6] JIA, Q., GU, D., “Selective laser melting additive manufacturing of Inconel 718 superalloy parts: densification, microstructure and properties”, *Journal of Alloys and Compounds*, v. 585, pp. 713–721, Feb. 2014. doi: <http://dx.doi.org/10.1016/j.jallcom.2013.09.171>.
- [7] WANG, P., LAO, C.S., CHEN, Z.W., *et al.*, “Microstructure and mechanical properties of Al-12Si and Al-3.5Cu-1.5Mg-1Si bimetal fabricated by selective laser melting”, *Journal of Materials Science & Technology*, v. 36, pp. 18–26, Jan. 2020. doi: <http://dx.doi.org/10.1016/j.jmst.2019.03.047>.
- [8] KUNZE, K., ETTER, T., GRÄSSLIN, J., *et al.*, “Texture, anisotropy in microstructure and mechanical properties of IN738LC alloy processed by selective laser melting (SLM)”, *Materials Science and Engineering A*, v. 620, pp. 213–222, Jan. 2015. doi: <https://doi.org/10.1016/j.msea.2014.10.003>.
- [9] WANG, P., CHEN, F.H., ECKERT, J., *et al.*, “Microstructural evolution and mechanical properties of selective laser melted Ti-6Al-4V induced by annealing treatment”, *Journal of Central South University*, v. 28, n. 4, pp. 1068–1077, 2021. doi: <http://dx.doi.org/10.1007/s11771-021-4680-3>.
- [10] XU, W., BRANDT, M., SUN, S., *et al.*, “Additive manufacturing of strong and ductile Ti-6Al-4V by selective laser melting via in situ martensite decomposition”, *Acta Materialia*, v. 85, pp. 74–84, Feb. 2015. doi: <https://dx.doi.org/10.1016/j.actamat.2014.11.028>.
- [11] ZHOU, L., MEHTA, A., MCWILLIAMS, B., *et al.*, “Microstructure, precipitates and mechanical properties of powder bed fused Inconel 718 before and after heat treatment”, *Journal of Materials Science & Technology*, vol. 35, n. 6, pp. 1153–1164, June 2018. doi: <https://doi.org/10.1016/j.jmst.2018.12.006>.
- [12] ZHANG, D., NIU, W., CAO, X., *et al.*, “Effect of standard heat treatment on the microstructure and mechanical properties of selective laser melting manufactured Inconel 718 superalloy”, *Materials Science and Engineering A*, v. 644, pp. 32–40, Sep. 2015. doi: <http://dx.doi.org/10.1016/j.msea.2015.06.021>.
- [13] ZHANG, Q.L., ZHANG, J., LI, D., *et al.*, “Microstructure and properties of laser additive remanufactured IN718 alloy with different aging temperatures”, *Rare Metal Materials and Engineering*, v. 49, pp. 8, 2020.
- [14] SHI, S.Y., ZHANG, Y.W., LV, X.D., “Effect of solid solution treatment on microstructure and stress rupture properties of Inconel 718 alloy fabricated by selective laser melting”, *Transactions of Materials and Heat Treatment*, v. 41, n. 6, pp. 8, 2020.
- [15] YOO, Y., BOOK, T.A., SANGID, M.D., *et al.*, “Identifying strain localization and dislocation processes in fatigued Inconel 718 manufactured from selective laser melting”, *Materials Science and Engineering A*, v. 724, pp. 444–451, 2018. doi: <http://dx.doi.org/10.1016/j.msea.2018.03.127>.
- [16] GALLMEYER, T.G., MOORTHY, S., KAPPES, B.B., *et al.*, “Knowledge of process-structure-property relationships to engineer better heat treatments for laser powder bed fusion additive manufactured Inconel 718”, *Additive Manufacturing*, vol. 31, pp. 100977, Jan. 2020. doi: <http://dx.doi.org/10.1016/j.addma.2019.100977>.
- [17] WANG, D., QIAN, Z.Y., DOU, W.H., *et al.*, “Research progress on selective laser melting of nickel based superalloy”, *Aeronautical Manufacturing Technology*, v. 61, n. 10, pp. 49–61, 2018.
- [18] NI, M., LIU, S., CHEN, C., *et al.*, “Effect of heat treatment on the microstructural evolution of a precipitation hardened superalloy produced by selective laser melting”, *Materials Science and Engineering, A*, vol. 748, pp. 275–285, Mar. 2019. doi: <https://doi.org/10.1016/j.msea.2019.01.109>.
- [19] COLLINS, P.C., BRICE, D.A., SAMIMI, P., *et al.*, “Microstructural control of additively manufactured metallic materials”, *Annual Review of Materials Research*, v. 46, n. 1, pp. 63–91, 2016. doi: <http://dx.doi.org/10.1146/annurev-matsci-070115-031816>.

- [20] HOLLAND, S., WANG, X., FANG, X.Y., *et al.*, “Grain boundary network evolution in inconel 718 from selective laser melting to heat treatment”, *Materials Science and Engineering A*, v. 725, pp. 406–418, 2018. doi: <http://dx.doi.org/10.1016/j.msea.2018.04.045>.
- [21] LIN, W.M., DUAN, J.F., WANG, C.L., *et al.*, “Research on precipitation strengthening of Ni-based superalloy”, *Foundry Technology*, v. 29, n. 5, pp. 3, 2008.
- [22] CHLEBUS, E., GRUBER, K., KUZNICKA, B., *et al.*, “Effect of heat treatment on the microstructure and mechanical properties of Inconel 718 processed by selective laser melting”, *Materials Science and Engineering A*, v. 639, pp. 647–655, 2015. doi: <http://dx.doi.org/10.1016/j.msea.2015.05.035>.
- [23] HOLLAND, S., WANG, X., FANG, X.Y., *et al.*, “Grain boundary network evolution in Inconel 718 from selective laser melting to heat treatment”, *Materials Science and Engineering: A*, vol. 725, pp. 406–418, May 2018. doi: <https://doi.org/10.1016/j.msea.2018.04.045>.
- [24] DOWLING, N.E., “Mechanical behavior of materials: engineering methods for deformation, fracture, and fatigue”, *International Journal of Fatigue*, vol. 19, no. 96, pp. 85, 1999.
- [25] SEIFI, M., SALEM, A., SATKO, D., *et al.*, “Defect distribution and microstructure heterogeneity effects on fracture resistance and fatigue behavior of EBM Ti–6Al–4V”, *International Journal of Fatigue*, vol. 94, Pt. 2, pp. 263–287, Jan. 2017. doi: <https://doi.org/10.1016/j.ijfatigue.2016.06.001>.
- [26] YU, X., LIN, X., WANG, Z., *et al.*, “Room and high temperature high-cycle fatigue properties of inconel 718 superalloy prepared using laser directed energy deposition”, *Materials Science and Engineering A*, vol. 825, pp. 141965, Sep. 2021. doi: <https://doi.org/10.1016/j.msea.2021.141865>.